A Robust Calibration Technique for Acoustic Emission Systems Based on Momentum Transfer from a Ball Drop

by Gregory C. McLaskey,[*] David A. Lockner, Brian D. Kilgore, and Nicholas M. Beeler

Abstract We describe a technique to estimate the seismic moment of acoustic emissions and other extremely small seismic events. Unlike previous calibration techniques, it does not require modeling of the wave propagation, sensor response, or signal conditioning. Rather, this technique calibrates the recording system as a whole and uses a ball impact as a reference source or empirical Green's function. To correctly apply this technique, we develop mathematical expressions that link the seismic moment M_0 of internal seismic sources (i.e., earthquakes and acoustic emissions) to the impulse, or change in momentum Δp, of externally applied seismic sources (i.e., meteor impacts or, in this case, ball impact). We find that, at low frequencies, moment and impulse are linked by a constant, which we call the force-moment-rate scale factor $C_{F\dot{M}} = M_0 / \Delta p$. This constant is equal to twice the speed of sound in the material from which the seismic sources were generated. Next, we demonstrate the calibration technique on two different experimental rock mechanics facilities. The first example is a saw-cut cylindrical granite sample that is loaded in a triaxial apparatus at 40 MPa confining pressure. The second example is a 2 m long fault cut in a granite sample and deformed in a large biaxial apparatus at lower stress levels. Using the empirical calibration technique, we are able to determine absolute source parameters including the seismic moment, corner frequency, stress drop, and radiated energy of these magnitude -2.5 to -7 seismic events.

Introduction

Extremely small seismic events, often called acoustic emissions (AEs), are associated with fracture, slip on frictional interfaces, and other processes occurring inside a material or structure. AEs produce mechanical vibrations that can be detected by sensors on the surface of the structure. This information is used to noninvasively monitor damage in engineering applications (e.g., Grosse and Ohtsu, 2008), in mining environments (e.g., Kwiatek et al., 2011), and for the laboratory study of rock fracture and faulting (e.g., Lockner, 1993) and semibrittle deformation (e.g., Brantut et al., 2011). For most AE monitoring applications, piezoelectric sensors with high sensitivity and recording systems with high gain are needed to ensure that large numbers of AEs are detected. However, the sensors and recording equipment are typically not calibrated, and it is not typically known whether a particular piezoelectric sensor measures acceleration, velocity, or displacement. This limits the usefulness and reliability of the method. AE systems that are not calibrated can be used to catalog the occurrence, locations, relative amplitudes, and, in some cases, the focal mechanisms of AEs, but physical inter-

pretations of the observations can be difficult. In contrast, systems that are calibrated allow users to determine the absolute amplitudes or size of the AEs, and this can help constrain their mechanics (McLaskey and Lockner, 2014). The assumed similarity between AEs and natural earthquakes provides one of the principal motivations for studying AE in the earth sciences (Mogi, 1962; Scholz, 1968; Lei et al., 1993; Goebel et al., 2012), but calibration is required to directly compare the size of AEs to their natural counterparts (Goodfellow and Young, 2014; McLaskey et al., 2014). Importantly, results from absolutely calibrated AE systems can be quantitatively compared to other AE results that employ different sensors and different recording equipment, and this will contribute to reliability and accountability of the method as a whole.

A fully calibrated AE system requires proper consideration of sensor response, the effects of filters and amplifiers, and elastodynamic wave propagation in the sample. A few researchers have calibrated AE systems either against theory (Eitzen and Brekenridge, 1987; McLaskey and Glaser, 2012) or using the principle of reciprocity (e.g., Hatano and Watanabe, 1997; Goujon and Baboux, 2003). Calibration experiments are typically performed on large, homogenous test blocks with simple geometry and polished surfaces. Because

*Now at Department of Civil and Environmental Engineering, Cornell University, Ithaca, New York 14853.

piezoelectric sensor response can change in different environments and when coupled to different materials or with different coupling methods, practitioners would prefer a relatively simple method to calibrate an AE system under conditions similar to those observed during an experiment or particular monitoring application (i.e., an *in situ* calibration).

In this article, we describe an *in situ* calibration method that allows us to make absolute measurements of AEs and other laboratory-generated seismic sources such as stick-slip events. Instead of calibrating the sensor, we calibrate the recording system as a whole, including the effects of wave propagation and sensor coupling. The method uses a tiny ball dropped onto the surface of the sample as a reference source, or empirical Green's function (EGF). The principle advantage of the ball impact source over other potential EGF sources such as small AEs, fracture of pencil lead or capillary tube, or piezoelectric pulses, is that the absolute amplitude of the seismic waves can be linked to the momentum of the ball, which is directly measured or easily estimated from the ball mass and drop height. The method relies on a number of simplifications and approximations, but because it does not require the practitioner to model wave propagation or sensor response, it is far simpler than alternative techniques. First, we present a theoretical formulation of the method. Then we demonstrate the technique on two different AE systems used for rock mechanics testing. Using the empirical calibration technique, we are able to determine absolute source parameters including the seismic moment, corner frequency, stress drop, and radiated energy.

Theoretical Formulation

The equations outlined below describe a mathematical framework for representing seismic signals based on the assumptions of linear transfer functions or linear systems theory (e.g., Hsu and Breckenridge, 1981; Oppenheim *et al.*, 1983). Throughout this article, we denote convolution in time by $\otimes$, subscripts designate vector and tensor components, a comma between subscripts designates a spatial derivative, and summation of repeated subscripts is implied. The superscripts int and ext indicate quantities pertaining to internal sources (e.g., earthquakes, AEs) and external sources (e.g., meteor impact, ball impact), respectively. We use a Green's function $g_{ki}(t)$ to represent the effects of wave propagation including geometrical spreading, scattering, and attenuation. Following previous work (e.g., Stump and Johnson, 1977; Aki and Richards, 1980), the spatial extent of the seismic source is approximated as a point, and the Green's function is expanded as a Taylor series about that point. Under this Taylor expansion, the real or equivalent forces that constitute the seismic source are represented by a force vector f_i and a series of moment tensors of increasingly higher order (i.e., m_{ij}, m_{ijl}, etc.), and ground displacement $u_k(t)$ is expressed as

$$u_k(t) = g_{ki}(t) \otimes f_i(t) + g_{ki,j}(t) \otimes m_{ij}(t)$$
$$+ g_{ki,jl}(t) \otimes m_{ijl}(t) + \dots . \tag{1}$$

For the characterization of earthquakes, underground explosions, mine collapse, acoustic emissions, and other seismic sources that are indigenous to the earth or specimen under test, conservation of linear momentum requires that $f_i = 0$, therefore only the second term of the Taylor series is used:

$$u_k^{\text{int}}(t) = g_{ki,j}^{\text{int}}(t) \otimes m_{ij}(t) = s^{\text{int}}(t) \otimes i_k^{\text{int}}(t)^{-1}. \tag{2}$$

The seismic source is represented by the (second order) moment tensor $m_{ij}(t)$, $s(t)$ refers to a recorded signal, and $i_k(t)$ is the instrument response function. For meteor impact (or ball impact) and other sources that act on the exterior of the earth (or laboratory sample), the first term of the Taylor series is used. Ground displacement is expressed as

$$u_k^{\text{ext}}(t) = g_{ki}^{\text{ext}}(t) \otimes f_i(t) = s^{\text{ext}}(t) \otimes i_k^{\text{ext}}(t)^{-1}, \tag{3}$$

and the seismic source is represented as a force vector $f_i(t)$.

Directionality of the Source

The directionality and spatial orientation of the source (the focal mechanism) is assumed to be separable from its amplitude and time history such that

$$\dot{m}_{ij}(t) = \dot{m}(t)\Lambda_{ij} = M_0 \dot{\hat{m}}(t)\Lambda_{ij} \tag{4}$$

and

$$f_i(t) = f(t)\Xi_i = \Delta p \hat{f}(t)\Xi_i. \tag{5}$$

Here, and throughout, variables with a hat refer to functions that retain the shape of their parent function (which have no hat) but have been normalized by their absolute amplitude (e.g., $\dot{\hat{m}}(t) = \dot{m}(t)/M_0$ and $\hat{f}(t) = f(t)/\Delta p$). Λ_{ij} is a tensor with the sum of the squares of the eigenvalues equal to 2 (e.g., Bowers and Hudson, 1999), Ξ_i is a vector of unit length, and M_0 and Δp are seismic moment and change in momentum as defined below. The overdot indicates a time derivative. Alternatively, directionality can be taken into account with radiation pattern terms (e.g., $\Lambda_{ij} = X^{SH}(\theta, \phi)$ and $\Xi_i = X^F(\phi)$), which adjust the amplitude of the source with the azimuth θ and dip ϕ of ray paths departing from the source. These radiation pattern effects are different for different wave phases (*P*, *SV*, *SH*) and source types (i.e., double couple versus point force).

In the current work, we average over multiple stations that sample θ and ϕ. This averages out the modulating effects of radiation pattern terms (i.e., $X_j \equiv \Xi_i / \Lambda_{ij} \approx 1$) and allows us to restrict the characterization of internal and external seismic sources to the estimation of $\dot{m}(t)$ or $f(t)$, respectively.

Empirical Green's Function Procedure

The current calibration procedure is based on the principle of an EGF (Mueller, 1985). In this approach, the source properties of one seismic event are estimated using a different, collocated event with a known or assumed source function as a reference. Instrument effects are never separated from wave propagation effects or radiation pattern. Instead, we define an instrument-apparatus response function

$$\psi^{\text{int}}(t) \equiv s^{\text{int}}(t) \otimes \dot{m}(t)^{-1} = \Lambda_{ij} \int g_{ki,j}^{\text{int}}(t)dt \otimes i_k^{\text{int}}(t) \qquad (6)$$

for a chosen source-sensor geometry and source focal mechanism. Similarly, for external sources,

$$\psi^{\text{ext}}(t) \equiv s^{\text{ext}}(t) \otimes f(t)^{-1} = \Xi_i g_{ki}^{\text{ext}}(t) \otimes i_k^{\text{ext}}(t). \qquad (7)$$

The time integral in equation (6) arises as a result of the time derivative associated with $\dot{m}(t)$.

In an EGF procedure, two events are compared. One acts as the EGF source (here denoted with the superscript EGF), and the other acts as the test source (superscript test). The relations below are outlined for internal sources only, but similar relations can be described for external sources. For brevity, we omit the superscripts int. The EGF and test events are collocated, recorded by the same seismic stations, and the focal mechanisms are assumed to be identical. Therefore,

$$\psi^{\text{EGF}}(t) = \psi^{\text{test}}(t). \qquad (8)$$

To solve for $\dot{m}^{\text{test}}(t)$, we first determine the instrument-apparatus response function $\psi^{\text{EGF}}(t)$ from recorded signals $s^{\text{EGF}}(t)$ using equation (6). Here, properties of the EGF source $\dot{m}^{\text{EGF}}(t)$ must be known or assumed. Then equation (8) is substituted into equation (6), and the source of the test event $\dot{m}^{\text{test}}(t)$ can be determined from recorded signals $s^{\text{test}}(t)$. This method has been used by numerous authors to study earthquakes (e.g., Frankel and Kanamori, 1983; Mueller, 1985; Hutchings and Wu, 1990; Hough and Dreger, 1995). A similar methodology has been employed for AEs (e.g., Dahm, 1996; Sellers *et al.*, 2003; Kwiatek *et al.*, 2011). For earthquakes, the absolute moment of the test event is often determined from an independently calibrated sensor network. For AEs, the magnitudes of both potential EGF and test events are unknown. In this work, we adapt the EGF technique so that we can use ball impact as an EGF source, because the absolute magnitude of the ball impact can be independently measured and its source spectrum is well known from theory. However, the impact source $f_i(t)$ is external to the body (equation 3) whereas the AE source $\dot{m}_{ij}(t)$ acts internally (equation 2), so we must derive an expression to relate internal and external sources, as described below.
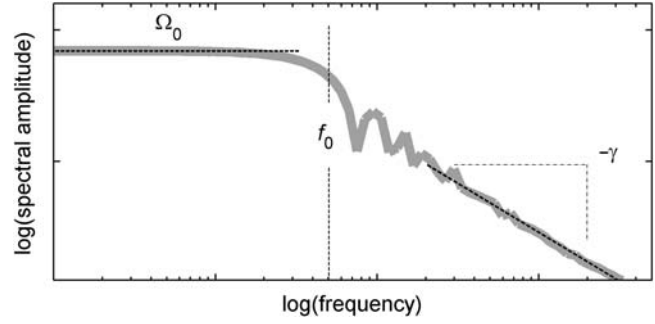

Figure 1. General features of the frequency spectrum of seismic sources include the low-frequency level Ω_0, the corner frequency f_0, and the high-frequency fall-off γ. For earthquakes and acoustic emissions (AEs), Ω_0 is equal to the seismic moment of the source, whereas for ball impact, it is equal to the ball's change in momentum.

Similarities between Spectra of Impacts and Earthquakes

An alternate and complementary way to describe a seismic source is by the characteristics of its frequency spectrum, which is determined from the Fourier transform of either $f(t)$ or $\dot{m}(t)$. In this approach, properties of the source are estimated in an average sense over the entire time window used to construct the Fourier transform. Phase information is generally ignored.

The basic features of the source spectra of impact sources, earthquakes, and AEs are described in Figure 1. Spectra of all of these types of sources are characterized by a corner frequency f_0 that is inversely proportional to T_d, the time duration of the nonzero part of $f(t)$ or $\dot{m}(t)$. For frequencies $f < f_0$, the spectra are flat and have long-period amplitude Ω_0. For $f > f_0$, spectra fall below Ω_0 with a high-frequency spectral decay of the form $(f/f_0)^{-\gamma}$. $\gamma = 2$ for most earthquake source models (e.g., Aki, 1967; Brune, 1970), whereas we find that $\gamma = 2.5$ for the ball impact (from the Fourier transform of $f(t)$ described by equation 17).

For the ball impact source, $f(t)$ is the force that the ball imposes on the surface of the specimen, and Ω_0 is proportional to the time integral of $f(t)$, which is the ball's change in momentum (due to change in velocity upon impact), or impulse, Δp. Similarly, $\dot{m}(t)$ is the moment rate of the earthquake, and Ω_0 is proportional to the time integral of $\dot{m}(t)$, which is the scalar seismic moment M_0. These low-frequency characteristics can be expressed in the frequency domain as

$$\dot{M}(f) = M_0 \qquad f < f_0 \qquad (9)$$

and

$$F(f) = \Delta p \qquad f < f_0. \qquad (10)$$

Even if the source is not ultimately described in the frequency domain, calculations are often performed in the frequency domain because convolution is reduced to multiplication. By taking their Fourier transforms, and using the

derivative theorem of Fourier transforms (Bracewell, 2000), equations (6) and (7) become

$$\Psi^{\mathrm{int}}(f) \equiv \frac{S^{\mathrm{int}}(f)}{\dot{M}(f)} = \frac{\Lambda_{ij} G_{ki,j}^{\mathrm{int}}(f) I_k^{\mathrm{int}}(f)}{i2\pi f} \qquad (11)$$

and

$$\Psi^{\mathrm{ext}}(f) \equiv \frac{S^{\mathrm{ext}}(f)}{F(f)} = \Xi_i G_{ki}^{\mathrm{ext}}(f) I_k^{\mathrm{ext}}(f), \qquad (12)$$

in which the instrument-apparatus response spectrum $\Psi(f)$ is the Fourier transform of the instrument-apparatus response function $\psi(t)$.

Relating Moment and Impulse

Noting that the spectra of $F(f)$ and $\dot{M}(f)$ are both flat at low frequencies, we propose that, under appropriate conditions, they are related by a simple constant. In particular, we are interested in determining the seismic moment of an internal source that has exactly the same ground displacement $u_k(t)$ as an external source of known impulse Δp (at least at frequencies below the corner frequency). This requirement, $u_k^{\mathrm{ext}}(t) = u_k^{\mathrm{int}}(t)$, defines the scale factor $C_{F\dot{M}}$ (for force-moment-rate):

$$C_{F\dot{M}} \equiv \dot{M}(f)/F(f) = \dot{m}(t)/f(t) = M_0/\Delta p \qquad f < f_0. \tag{13}$$

$C_{F\dot{M}}$ has units of velocity and is equal to twice the wave velocity in the material from which the seismic sources originate. If S waves (P waves) are used to estimate M_0 and Δp, then $C_{F\dot{M}}$ is twice the S-wave (P-wave) velocity. $C_{F\dot{M}}$ is derived theoretically in the Appendix, and is verified experimentally as described in the Empirical Estimation of $C_{F\dot{M}}$ section.

To relate $\psi^{\mathrm{ext}}(t)$ and $\psi^{\mathrm{int}}(t)$, we substitute equation (13) into equation (6) to obtain

$$s^{\mathrm{int}}(t) = C_{F\dot{M}} f(t) \otimes \psi^{\mathrm{int}}(t) \qquad f < f_0. \tag{14}$$

For the special case when internal and external sources have identical ground displacements, $u_k^{\mathrm{ext}}(t) = u_k^{\mathrm{int}}(t)$, and they are recorded on identical instruments, $i_k^{\mathrm{ext}}(t) = i_k^{\mathrm{int}}(t)$, then their recorded signals are also identical, $s^{\mathrm{ext}}(t) = s^{\mathrm{int}}(t)$ (at frequencies below the corner frequency). In this case, we equate equation (14) with equation (7) to find

$$\psi^{\mathrm{ext}}(t) = C_{F\dot{M}} \psi^{\mathrm{int}}(t) \qquad f < f_0. \tag{15}$$

In the frequency domain, this becomes

$$\Psi^{\mathrm{ext}}(f) = C_{F\dot{M}} \Psi^{\mathrm{int}}(f) \qquad f < f_0. \tag{16}$$

Equations (13), (15), or (16) can be used to relate properties of internal seismic sources (e.g., earthquakes, AEs) to properties of external seismic sources (meteor impact, ball impact). For example, the equations can be used to find the equivalent seismic moment of a meteor impact (the seismic moment of a collocated earthquake that would produce the same low-frequency ground motions) or the equivalent change in momentum of an earthquake or AE.

Determination of Force-Time Function $f(t)$ Using Hertz Theory

Following previous work, the force-time history, $f(t)$, that a ball imposes upon a massive body can be calculated from Hertzian theory. This theory relies on the mechanics of elasticity to derive forces and deformation associated with the collision of spheres. McLaskey and Glaser (2010) showed that, despite its quasistatic and elastic form, Hertzian theory adequately describes the force pulses and resulting stress waves that arise from the collision of small balls on massive samples composed of a variety of materials. In the following equations, $\delta_I = (1 - \mu_i^2)/(\pi E_i)$, and E and μ are the Young's modulus and Poisson's ratio, respectively. R_1 and v_0 are the radius and incoming velocity of the ball. Subscript 1 refers to the material of the ball and subscript 2 is the material of the more massive test specimen. The time the ball spends in contact with the specimen is $t_c = 1/f_c = 4.53(4\rho_1\pi(\delta_1 + \delta_2)/3)^{2/5} R_1 v_0^{-1/5}$, and the maximum force the ball exerts during this time is $F_{\mathrm{max}} = 1.917\rho_1^{3/5}(\delta_1 + \delta_2)^{-2/5} R_1^2 v_0^{6/5}$ (Goldsmith, 2001; McLaskey and Glaser, 2010, 2012). The full force-time function is

$$\begin{array}{ll} f(t) = F_{\mathrm{max}} \sin(\pi t/t_c)^{3/2} & 0 \le |t| \le t_c, \\ f(t) = 0 & \text{otherwise} \end{array} \tag{17}$$

The change in momentum Δp that the ball imparts to the test specimen is equal to the area under the force-time function $\Delta p \approx 0.5564 t_c f_{\mathrm{max}}$. Δp can be independently calculated based on the mass m of the ball and the incoming (v_0) and rebound (v_f) velocities: $\Delta p = m(v_0 - v_f)$ (v_0 and v_f have opposite signs). In this work, we refer to the impact as ball impact rather than elastic impact because we find that it need not be completely elastic. If the ball rebounds to greater than half of the original drop height then its source characteristics can be adequately estimated from the above equations as long as F_{max} is scaled to account for the diminished change in momentum Δp. For example, if the ball bounces back to half its original drop height, then the maximum force $F_{\mathrm{max}\,1/2} \approx 0.75 F_{\mathrm{max}}$.

Summary of the Method

To estimate the absolute source properties of an AE, we must deconvolve the path and instrument effects (represented by $\Psi^{\mathrm{int}}(f)$) from recorded signals $s^{\mathrm{int}}(t)$. We cannot obtain $\Psi^{\mathrm{int}}(f)$ directly from recorded AE signals because the absolute amplitude of a suitable EGF event is typically not available. Instead, we employ the force-moment-rate scale factor
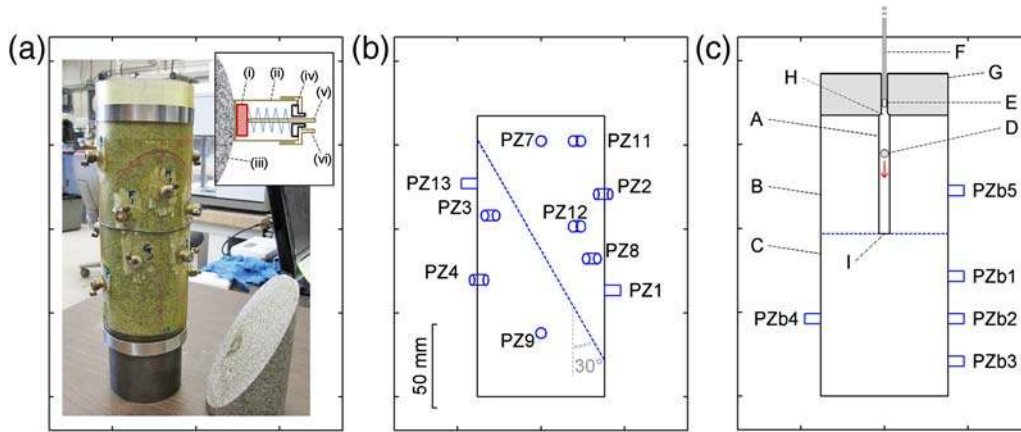
Figure 2. (a) Photo of the granite sample and sensors. (b) Schematic of the test sample shows the saw-cut simulated fault (dashed line) that slips to produce AEs. (c) The calibration sample contains a cavity in which the ball is dropped by means of a tiny magnet attached to a wire (see the Example 1: Triaxial Apparatus section). Piezoelectric AE sensors are shown as cylinders (PZ1–PZ16 and PZb1–PZb5). As depicted in the inset of (a), each sensor consists of a cylindrical piezoceramic element (i) 6.35 mm in diameter and 2.54 mm thick and composed of lead–zirconate–titanate (PZT). This is soldered inside a brass cup (ii) that is machined to match the sample curvature and is glued directly on the granite sample (iii). A spring supplies force to the back of the PZT element, and a teflon insulator (iv) separates the signal (v) from the ground (vi). When inside the pressure vessel, confining fluid fills the inside of the brass cup. The color version of this figure is available only in the electronic edition.

$C_{F\dot{M}}$ (equation 16) to derive the desired instrument-apparatus response ($\Psi^{\text{int}}(f)$) from that of a collocated ball drop ($\Psi^{\text{ext}}(f)$). We can obtain $\Psi^{\text{ext}}(f)$ directly from signals recorded from a ball impact $s^{\text{ext}}(t)$ (equation 12) because the absolute source spectrum of the ball drop ($F(f)$) can be obtained from the Fourier transform of the ball's force-time function, which can be calculated from Hertz theory (equation 17).

Example 1: Triaxial Apparatus

In this first example, we demonstrate the empirical calibration technique on a cylindrical sample of Westerly granite (76.2 mm diameter) in a triaxial loading apparatus at a confining pressure of 40 MPa. During a typical experiment, AEs are produced by deformation on a simulated fault that is a saw cut inclined at 30° to the vertical axis, as shown in Figure 2a,b. The saw-cut surfaces were surface ground and then hand lapped with 600 grit abrasive (approximately 15 μm particle size) to produce a smooth, uniform fault surface. The test sample is instrumented with 16 AE sensors (PZ1–PZ16) described in detail in Figure 2. The granite sample is enclosed in a polyurethane jacket to isolate it from the silicone oil used as the confining fluid. More experimental details can be found in McLaskey and Lockner (2014).

To estimate the absolute amplitude of the AEs with the empirical calibration method, we need to employ equation (16). For this equation to be valid, we must perform a ball drop under conditions that are nearly identical to those of the AEs. To accomplish this for AEs produced by a sample inside a pressure vessel, we assembled a calibration sample, shown schematically in Figure 2c. The calibration sample is identical to the test sample (Fig. 2b), except that instead of a simulated fault, it contains a cavity in which ball impact can take place. To prepare the calibration sample, a 76.2 mm

diameter granite cylinder was cut perpendicular to its axis. A 6.35 mm diameter hole (A) is drilled down the center axis of one piece (B). The other piece (C) is kept intact, and they are surface ground and epoxied back together. A 4.76 mm diameter steel ball (D) is placed in the hole. A 3.2 mm diameter magnet (E) is glued to the end of a 300 mm long section of piano wire (F). A cylindrical steel end cap (G) 25 mm long and 76 mm in diameter has a hole in its center, and a hollow cylindrical aluminum insert is glued into this hole that is large enough to allow the wire and magnet to pass through but small enough to stop the ball. The piano wire extends out of the hole and out of the pressure vessel through a section of tubing. By manually pushing on the piano wire, the magnet can be lowered to the bottom of the hole. The steel ball adheres to the magnet, and, by pulling on the wire, it can be lifted to the top of the hole (H). At this point, the ball is stopped by the aluminum insert, the magnet is pulled away from the ball, and the ball falls 66.5 mm onto the sample surface (I). Seismic waves radiated from the point of impact propagate through the sample and are recorded by piezoelectric sensors (PZb1–PZb5) glued directly on the granite sample. The ball imposes some force to the sample at position (H) when it is pulled away from the magnet. This force acts too slowly to generate kilohertz-frequency seismic waves, and it is separated in time by the >100 ms of time spent in the air as the ball falls from position (H) to the location of impact at position (I), so it does not contaminate recorded ground motions.

EGF and Test Spectra $S^{\text{ext}}(f)$ and $S^{\text{int}}(f)$

We compare signals from the ball impact described above to those from AEs located near the center of the test sample. Because ball impact and AEs are essentially collocated, this
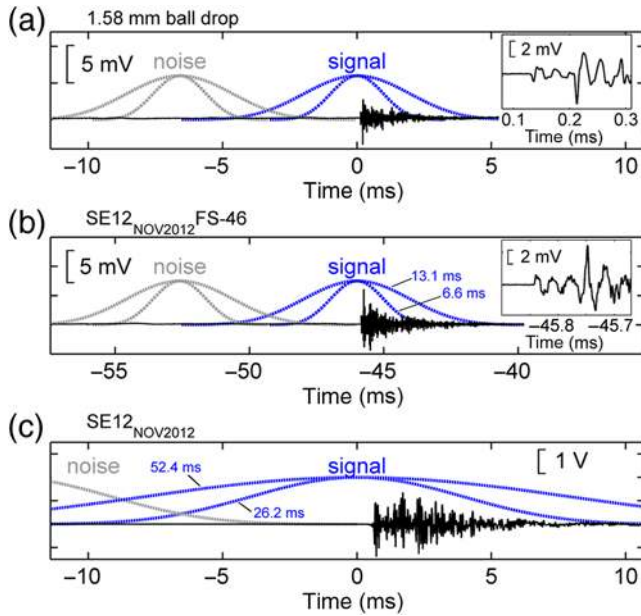
Figure 3. Illustration of windowing technique for obtaining spectra. Spectra are derived from sections of recorded signals (black) centered on the first-wave arrival and tapered with a Blackman Harris window. This is compared to noise spectra derived from an earlier part of the signal. We always compare spectral estimates derived from time windows of various lengths T_{wind}. Four example window lengths are shown. For the (a) small ball drop and (b) small AE event, we show $T_{wind} = 6.6$ and 13.1 ms. For the largest laboratory-generated seismic events, such as the stick-slip event shown here, we employ longer time windows. The three example events shown were generated in the large biaxial apparatus. Following the notation of McLaskey *et al.* (2014), events are labeled by their timing relative to the initiation of the stick-slip instability. For example, SE12Nov2012FS-46 is a foreshock that occurred 46 ms before the initiation of the twelfth stick-slip instability of a sequence generated in November 2012. The source locations of the (a) ball impact and (b) small AE are depicted in Figure 7, and the signals shown are the recordings from sensors PZ4 and PZ5, respectively. A zoom in of the first arrivals of these signals is shown in the insets. The color version of this figure is available only in the electronic edition.
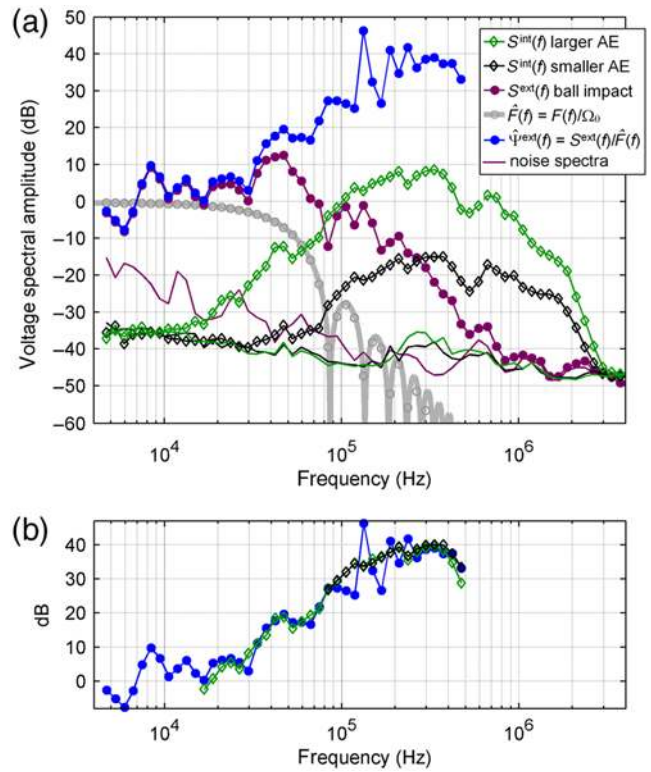

Figure 4. (a) Spectra of two collocated AEs (diamonds) and a collocated ball impact (circles) are shown against corresponding noise spectra (lines without symbols near the bottom of the plot). The theoretical source spectrum of the ball impact derived from Hertz theory is shown in light gray. Also shown is the instrument-apparatus response spectrum, which is derived by dividing the raw spectrum of the ball impact by the theoretical spectrum of the ball impact. (b) The spectra of the two AEs are offset vertically to match the ball-impact-derived instrument-apparatus response spectrum in the low-frequency range in which there is good signal-to-noise ratio. This offset is used to determine the seismic moment of the AEs from the change in momentum of the ball impact. The color version of this figure is available only in the electronic edition.

ensures that signals recorded from ball impact and AEs have experienced nearly identical wave propagation and instrument response effects. Though the radiation patterns of the impact and AEs are different, we minimize these differences by deriving spectra from the average of signals from many sensors, and we choose combinations of sensors with source-to-sensor ray-path lengths and incidence angles that are similar between the ball drop and the AE.

In this article, spectra are obtained from the absolute value of the Fourier transform of a section of a recorded waveform that is centered on the first-wave arrival and tapered with a Blackman–Harris window, as depicted in Figure 3. This is compared to noise spectra derived using a window of identical length and taper but from a section of the recorded waveform before the first-wave arrival. We analyze spectra obtained from windows of various lengths ($T_{wind} = 3.3, 6.6, 13.1, 26.2$ ms, etc.), and we keep only spectral estimates in a frequency band

where estimates are consistent over multiple time windows and have sufficient signal-to-noise ratio (SNR). Signal sections are relatively long and include both P and S arrivals as well as coda. Spectra are resampled into equal intervals in log frequency at $\Delta \log_{10}(f) = 0.025$ or 0.05. Each resampled spectral estimate (shown as symbols in Figs. 4, 5, and 6) is the average of spectral estimates from at least two Fourier frequencies. For cases for which SNR is favorable even at the lowest frequencies, the lower limit of spectral estimates is $f_{min} = 20/T_{wind}$. The upper bound of spectral estimates is always limited by SNR rather than recording bandwidth. We are careful to use identical windowing techniques on both the ball drop (EGF) and AE (test) data.

Figure 4a shows the amplitude of raw spectra $S^{int}(f)$ of two different AE events located close to the center of the sample. These spectra are shown with corresponding noise spectra to illustrate the frequency-dependent nature of signal-to-noise ratio. The spectra shown are the average of spec-
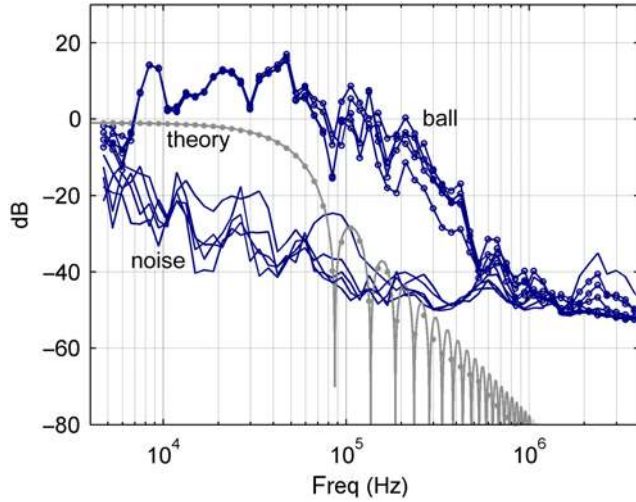
Figure 5. The spectra of five ball drop sources performed in the calibration sample inside the pressure vessel of a triaxial apparatus at 40 MPa confining pressure. The lower curves without symbols are corresponding noise spectra. The shape of the theoretical source spectrum (light gray) is shown for comparison. Below the corner frequency, the spectra of all ball drops are identical to within 2 dB. Above the corner frequency, spectra vary by up to 10 dB, so averages of five ball drops are shown in Figures 4 and 6b. The color version of this figure is available only in the electronic edition.

tra derived from 11 different sensors' recordings. The 11 sensors have an average source-to-sensor path length of 58 mm and average incidence angle of 49°.

Figure 4a also shows the amplitude of the raw spectrum $S^{\mathrm{ext}}(f)$ of a ball impact performed inside the calibration sample at 40 MPa confining pressure. In the frequency band below f_0, spectra derived from signals from different ball drops are identical to within 2 dB, as described in Figure 5. Above f_0, spectral amplitudes at a given frequency may vary by as much as 10 dB between different ball drops performed under nominally identical conditions (presumably due to variation in the details of the impact, such as the effects of microscale surface topography and surface contaminants). To obtain more stable spectral estimates, we calculate spectra $S^{\mathrm{ext}}(f)$ from the average of spectra from five different ball drops. In addition to averaging over five ball drops, $S^{\mathrm{ext}}(f)$ shown in Figure 4 is the weighted average of spectra estimated from recordings at three stations (PZb1, PZb2, and PZb3, see Fig. 2c). The weighted average ray-path length (59 mm) and incidence angle (50°) are nearly identical to those from signals used to calculate the spectra of the AE signals $S^{\mathrm{int}}(f)$.

Figure 4a also includes $\hat{F}(f) = F(f)/\Delta p$, which is the spectrum of the impact source that we calculated theoretically using Hertz theory (equation 17) for the characteristics of the current ball drop (4.76 mm diameter steel ball dropped 66 mm onto granite) normalized by its long-period level $\Delta p = m(v_0 + v_f) = 1 - 10^{-3}$ N·s. Here, m is the mass of the 4.76 mm diameter ball (0.432g), v_0 is the incoming velocity of the ball, and v_f is the rebound velocity of the ball. We calculate $v_0 = 1.2$ m/s from the 66.5 mm drop height,

and we estimate $v_f = 1.0$ m/s from the 209 ms of travel time in air between the first and second bounces of the ball, which we can determine based on a long-time recording of seismic waves generated from two successive bounces. (Time windows used to obtain spectra include only one bounce.)

Instrument-Apparatus Response and Absolute Moment

The instrument-apparatus response spectrum $\hat{\Psi}^{\mathrm{ext}}(f)$ is derived from equation (12)

$$\hat{\Psi}^{\mathrm{ext}}(f) = S^{\mathrm{ext}}(f)/\hat{F}(f) = \Delta p \Psi^{\mathrm{ext}}(f) \qquad (18)$$

and is also shown in Figure 4.

Figure 4b shows $\hat{\Psi}^{\mathrm{ext}}(f)$ alongside the raw spectra $S^{\mathrm{int}}(f)$ of the two AEs. The slopes and shapes of these spectra are similar, and the AE spectra have been offset vertically by 31 and 55 dB to match $\hat{\Psi}^{\mathrm{ext}}(f)$ at low frequencies. (Only the frequency band with sufficient SNR is shown. Also note that the spikes in $\hat{\Psi}^{\mathrm{ext}}(f)$ at about 150 and 200 kHz are the result of troughs in the ball drop spectrum $F(f)$ that have not been entirely erased by spectral resampling.) The seismic moment of the AEs can be calculated from the vertical offset between the AE spectra and the ball-drop-derived instrument-apparatus response spectrum $\hat{\Psi}^{\mathrm{ext}}(f)$. To accomplish this, we substitute equation (9) into equation (11) to find

$$S^{\mathrm{int}}(f) = M_0 \Psi^{\mathrm{int}}(f), \qquad f < f_0. \qquad (19)$$

Then, we substitute equation (16) into equation (18) and divide the result by equation (19) to find

$$\frac{\hat{\Psi}^{\mathrm{ext}}(f)}{S^{\mathrm{int}}(f)} = \frac{\Delta p \Psi^{\mathrm{ext}}(f)}{M_0 \Psi^{\mathrm{int}}(f)} = \frac{\Delta p C_{F\dot{M}}}{M_0}. \qquad (20)$$

We then replace variables with numerical values and solve for M_0. For the larger AE, $\hat{\Psi}^{\mathrm{ext}}(f)/S^{\mathrm{int}}(f) = 31$ dB $= 35$ (20 dB equals a factor of 10), so $M_0 = \Delta p \times C_{F\dot{M}}/35 = 1$ mN·s $\times$ 10 km/s/35 $= 0.3$ N·m. We use the relation $\mathbf{M} = 2/3 \times \log_{10}(M_0) - 6.067$ (Hanks and Kanamori, 1979) to find the AE moment magnitude $\mathbf{M} -6.4$. Similarly, the smaller AE has a moment of 0.02 N·m ($\mathbf{M} -7.2$).

As described in the Appendix, we find that $C_{F\dot{M}}$ is approximately equal to twice the wave velocity. Because spectra are derived from the Fourier transforms of time windows that include both P and S waves, we choose the average of the P-(c_P) and S-wave velocities (c_S) and calculate a force-moment-rate constant $C_{F\dot{M}} = 2(c_P + c_S)/2 = 10$ km/s for the Westerly granite under 40 MPa confining pressure.

Effects of Confining Pressure

The calibration sample described above also allows us to assess how the instrument-apparatus response spectrum $\Psi^{\mathrm{ext}}(f)$ changes with confining pressure and with the pres-
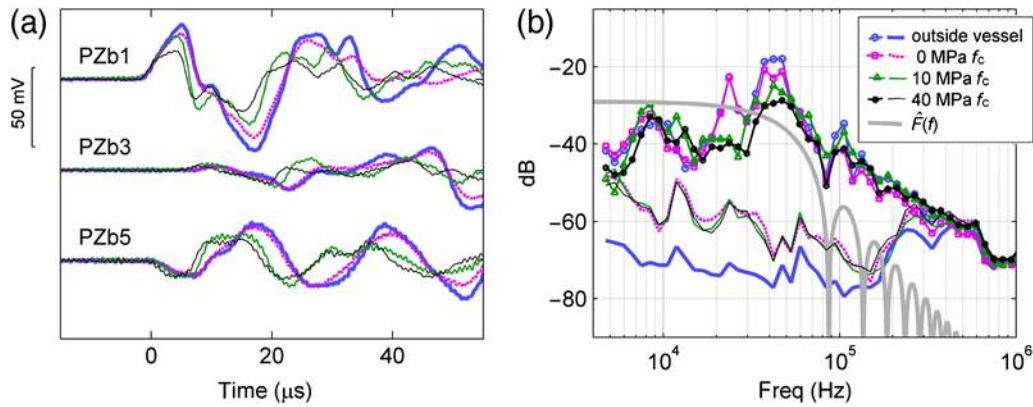
Figure 6. The ball drop allows us to assess how wave propagation and sensor response are affected by increases in confining pressure. (a) Raw waveforms and (b) spectra show that increasing confining pressure increases the velocity in the sample and dampens resonant peaks in the sensor response spectrum. In (b), the spectral estimates (symbols) are shown relative to corresponding noise spectra (lower four curves without symbols). The enhanced damping could be the result of improved acoustic coupling between the back of the PZT element and the confining oil. The shape of the theoretical ball impact source spectrum $\hat{F}(f)$ (offset vertically) is shown in light gray for reference. The color version of this figure is available only in the electronic edition.

ence of confining fluid. Because the force-time history $f(t)$, that the ball imposes on the sample, is essentially constant between different ball drops, changes in recorded signals $s^{\text{ext}}(t)$ can be attributed to changes in instrument-apparatus response $\psi^{\text{ext}}(t)$. Raw recorded signals and spectra are shown in Figure 6 for ball drops conducted at different values of confining pressure.

The recorded waveforms show that increasing confining pressure has two main effects. First, the velocity in the material increases, as evidenced by earlier wave arrivals and an overall contraction of the waveforms in time (Fig. 6a). Second, the amplitude of the signals decreases. In the frequency domain, increased confining pressure appears to diminish the amplitude of resonant peaks in the spectra (at 22, 40, and 100 kHz). The largest changes occur when confining pressure is increased from 0 to 10 MPa. Further increases from 10 MPa to 40 MPa introduce less significant changes. (Note that although spectra shown in Figure 6b are the average of spectra derived from PZb1 through PZb5, spectra derived from individual sensor's recordings have nearly identical features.)

Overall, we find that confining pressure and confining fluid have relatively minor effects on sensor response and primarily appear to dampen resonant peaks, at least in our ~5–500 kHz reliable frequency band, from which we have good SNR. This suggests that bench-top calibrations performed when the sample is outside the pressure vessel may be adequate for a rough (order of magnitude) calibration of these particular AE sensors.

Example 2: Large-Scale Biaxial Apparatus

Next, we demonstrate the use of the empirical calibration technique on a large, biaxial apparatus shown in Figure 7. The apparatus accommodates a granite sample that is 1.5 m square and 0.4 m thick. Deformation is accommodated on a 2 m long simulated fault that is saw-cut diagonally through the sample,

shown as the dashed line in Figure 7. The sample is instrumented with 15 Panametrics V103 piezoelectric sensors. Further details are described in McLaskey and Kilgore (2013) and McLaskey et al. (2014).

In the previous example, we estimated the instrument-apparatus response spectrum $\Psi^{\text{ext}}(f)$ from a single ball drop with a given mass, but here we record many different ball drops with a wide variety of ball sizes. This allows us to broaden the frequency band over which the instrument-apparatus response can be reliably estimated. Second, and for convenience, we analyze AE and ball drop EGF pairs that are not precisely collocated. We do not drill a hole in the sample, and hence the ball impact occurs on the top surface of the sample, where it is easily accessible, and AEs occur on the saw-cut simulated fault. This can potentially decrease the accuracy of the method, but we argue that the technique is still useful for estimating the general features of the AE source spectra, especially if estimates can be made over a very broad frequency band. As illustrated in Figure 7, we take advantage of the symmetry of the test sample to provide ray paths that are geometrically similar for ball drops and corresponding AEs. By choosing sets of signals with average ray-path lengths and takeoff angles that are similar between the ball impact and AE sources, as depicted in Figure 7, we maintain the general validity of equation (16). Further details about steps taken to reduce errors associated with AE-ball-drop EGF pairs that are not collocated are described in the Applicability of $\Psi^{\text{int}}(f) = C_{F\dot{M}}\Psi^{\text{ext}}(f)$ section.

Instrument-Apparatus Response

Figure 8a shows the amplitude of spectra $S^{\text{ext}}(f)$ of collocated ball impacts of various sizes, listed in Table 1. All balls are dropped from a height of 1 m onto the top surface of the granite sample while 5 MPa normal stress and 3 MPa shear stress is applied to the fault to simulate actual test
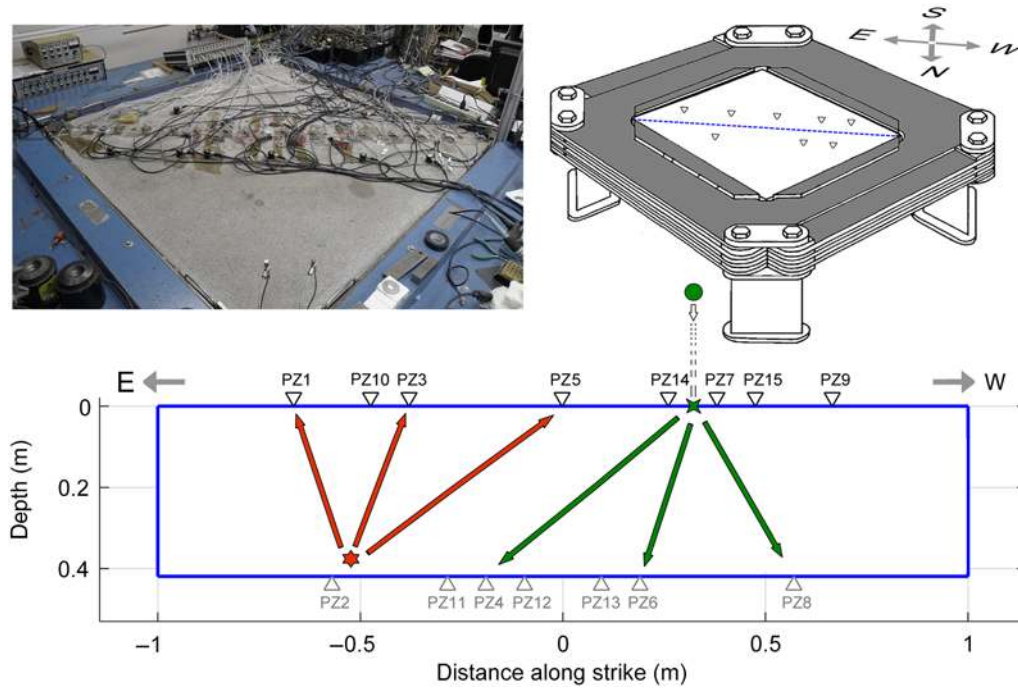
Figure 7. (top) A photo and a sketch of the large granite sample in a biaxial loading frame. Triangles denote the locations of piezoelectric AE sensors. (bottom) A zoom in on the fault cross section showing sensor locations and example source locations. The ball (circle) is dropped from a height of one meter onto the top surface of the specimen (four-pointed star) and AEs under analysis occur on the fault surface (six-pointed star). Although the ball drop and AEs are not collocated, we derive spectra from signals from sensors with ray-path lengths, angles, and propagation characteristics that are similar between the ball drop and AE. The color version of this figure is available only in the electronic edition.

conditions. Figure 8b shows the same spectra, but the amplitudes of each of the spectra are offset by the respective Δp calculated for each particular ball drop. For frequencies sufficiently below f_0, all the offset spectra collapse to a single curve that defines the instrument-apparatus response spectrum $\Psi^{\text{ext}}(f)$. (Mathematically, we substitute equation 10 into equation 7 and Fourier transform the result to find $\Psi^{\text{ext}}(f) = S^{\text{ext}}(f)/\Delta p$.) We combine the results from the different ball sizes to construct an estimate of $\Psi^{\text{ext}}(f)$ over a wide frequency band in a method inspired by that of Baltay *et al.* (2010). Next, we divide individual raw spectra ($S^{\text{ext}}(f)$) by this newly derived instrument-apparatus response spectrum ($\Psi^{\text{ext}}(f)$) to obtain an estimate of the source spectra $F(f)$. Figure 8c shows $F(f)$ of four ball impact sources of different sizes alongside the theoretical impact force spectra derived from Hertzian theory (equation 17).

Source Spectra of Laboratory-Generated Earthquakes

Figure 9a shows the amplitude of spectra $S^{\text{int}}(f)$ of eight laboratory-generated seismic events of various sizes. Although the smaller events ruptured localized patches of the fault surface and can be classified as AEs, we refer to them as laboratory-generated seismic events rather than simply AEs: the two largest amplitude events are from the complete rupture of the entire 2 m long simulated fault and are generally referred to as stick-slip instabilities. The smaller events are

from foreshocks and aftershocks of various sizes that occur in the milliseconds before and after the stick-slip instability. The rupture areas of these events are fully contained within the fault surface and do not break out to the fault boundaries.

Figure 9b shows the spectra presented in Figure 9a divided by the instrument-apparatus response $\Psi^{\text{ext}}(f)$ derived from ball impact $S^{\text{int}}(f)/\Psi^{\text{ext}}(f) = F(f)$. (This result is obtained by substituting equation 15 into equation 14 and Fourier transforming the result.) The left axis of Figure 9b shows the equivalent momentum change Δp_{equiv} that corresponds to the low-frequency level Ω_0 of $F(f)$ of the laboratory-generated events. Using equation (13), we can convert $F(f)$ into $\dot{M}(f)$. The right axis label shows $M_0 = C_{F\dot{M}}\Delta p_{\text{equiv}}$. (Here, we use $C_{F\dot{M}} = 2(c_P + c_S)/2 = 7$ km/s, for Sierra White granite samples under ~5 MPa stress levels.) To aid interpretation, we also display four theoretical source spectra derived from the Brune (1970) earthquake source model

$$\dot{M}_{\text{Brune}}(f) = M_0/(1 + (f/f_0)^2). \tag{21}$$

From the spectra shown in Figure 9b, we find that the largest events that rupture the entire fault have M_0 of approximately 2×10^5 N·m (**M** −2.5). The largest foreshocks (Patch P1 foreshocks in the terminology of McLaskey and Kilgore, 2013) have M_0 of about 100 N·m (**M** −4.5 to **M** −5). Smaller foreshocks and aftershocks have M_0 ranging from 0.1 to 1 N·m (**M** −6 to **M** −7) and are similar in
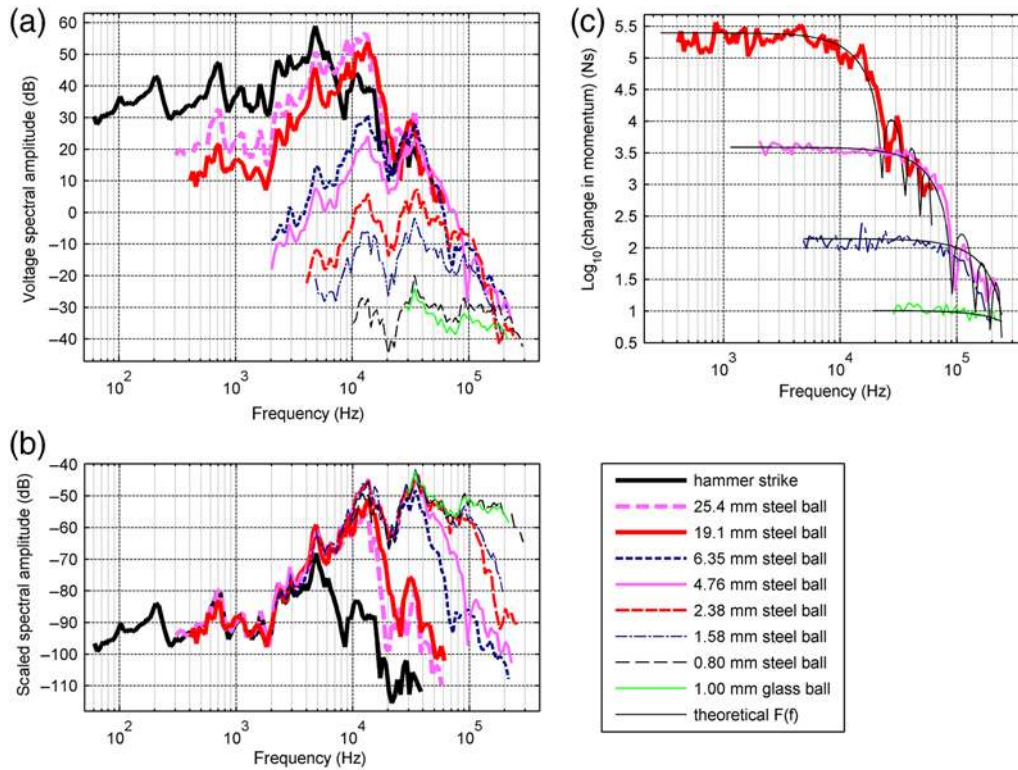
Figure 8. Spectra from a suite of collocated ball drops with different sized balls. (a) Spectra shown are the amplitude of the average of spectra derived from recordings from three sensors with source-to-sensor distances of 0.63, 0.44, and 0.53 m. Larger sized balls have systematically larger low-frequency amplitudes, and a lower corner frequency f_0. (b) When the spectra are offset vertically by the measured change in momentum of each ball, the spectra at frequencies less than f_0 collapse to a single curve that defines the instrument-apparatus response spectrum. (c) The instrument-apparatus response spectrum is removed from the spectra of four different ball drop sources to produce an estimate of the true source spectra. These estimates are shown alongside theoretical spectra derived from Hertz theory (thin black lines). The color version of this figure is available only in the electronic edition.

size to the AEs generated with the triaxial apparatus discussed previously.

Empirical Estimation of $C_{F\dot{M}}$

The large and simple geometry of the 2 m sample also facilitates quantitative time-domain analysis of the smaller foreshocks and aftershocks using the waveform modeling approach of McLaskey *et al.* (2014), and this allows us to empirically estimate the scale factor $C_{F\dot{M}}$. The waveform

modeling approach requires the estimation of Green's functions and the sensors' instrument response function $i(t)$. These are needed for the construction of synthetic seismograms that can be compared to recorded signals. We first determine M_0 from waveform modeling (see McLaskey *et al.*, 2014). Then we estimate the equivalent change in momentum Δp_{equiv} from the low-frequency level of the spectra as plotted in Figure 9b. Once both Δp_{equiv} and M_0 have been estimated for a single event, we estimate $C_{F\dot{M}}$ from equa-

Table 1
Properties of Ball Drops Shown on Figure 8

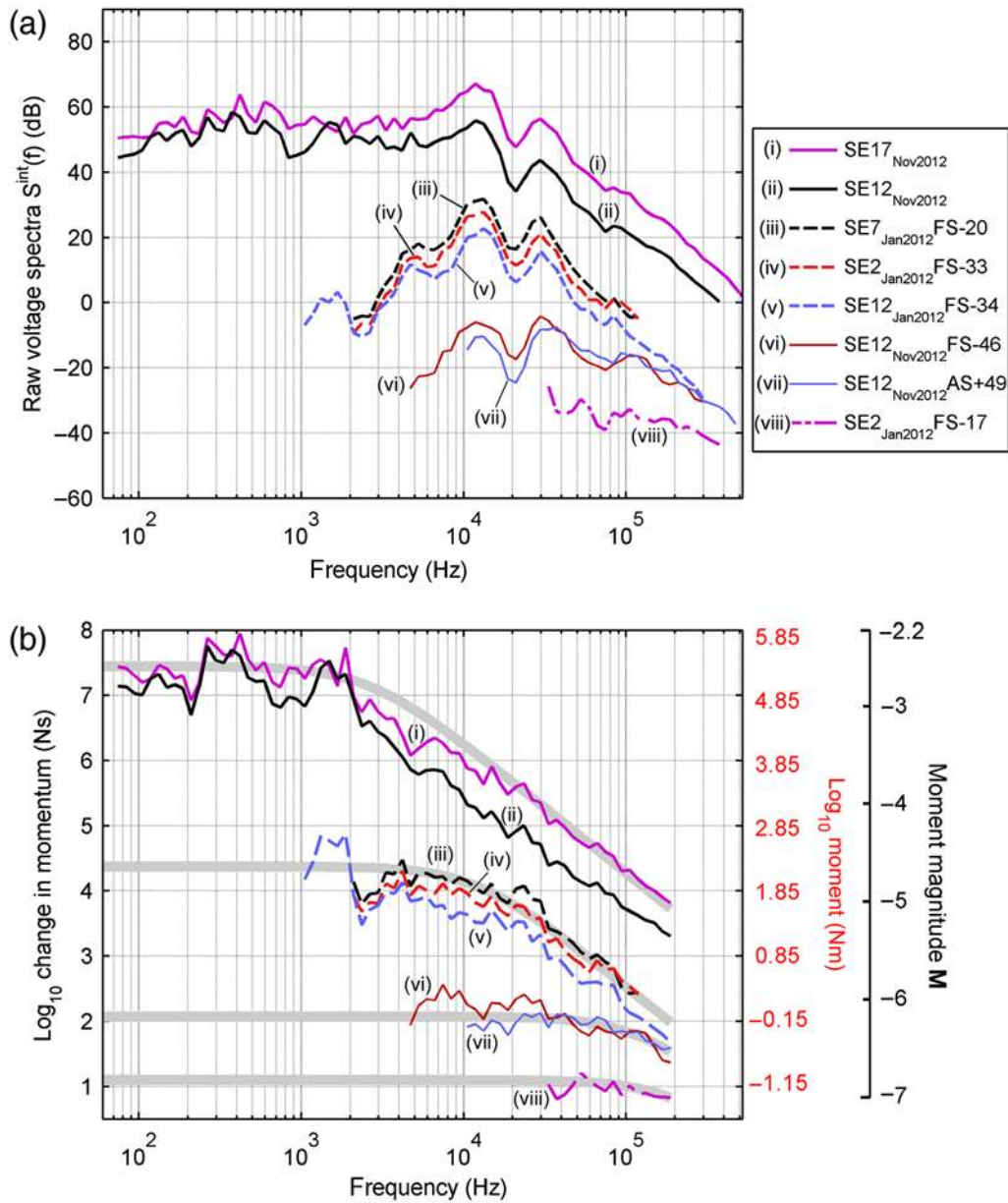| Ball Diameter (mm)	Material	Mass (g)	Corner Frequency (kHz)	Change in Momentum (N·s)	Equivalent M
0.80	Steel	0.0021	300	1.6×10^{-5}	−6.7
1.00	Glass	0.0013	345	9.8×10^{-6}	−6.8
1.58	Steel	0.016	156	1.2×10^{-4}	−6.1
2.38	Steel	0.055	100	4.1×10^{-4}	−5.7
4.76	Steel	0.44	52	3.3×10^{-3}	−5.1
6.35	Steel	1.05	39	7.9×10^{-3}	−4.9
7.94	Steel	2.06	31	1.5×10^{-2}	−4.7
19.1	Steel	28.4	13	2.1×10^{-1}	−3.9
25.4	Steel	67.4	9.7	5.0×10^{-1}	−3.7
Hammer strike	Steel	n/a	n/a	$2.7 \times 10^{+0}$	−3.2

Figure 9. (a) The amplitude of raw spectra from eight laboratory-generated seismic events of different sizes. The two largest events are from stick-slip instabilities that rupture the entire 2 m long fault. The smaller events are foreshocks (FS) and aftershocks (AS), which occur in the milliseconds surrounding the large instabilities. (b) The same spectra are divided by the instrument-apparatus response spectrum (from Fig. 8) to obtain estimates of source spectra. Thick gray lines are example Brune source models (see the Source Dimension, Stress Drop, and Radiated Energy section). The event naming scheme is consistent with Figure 3 and McLaskey *et al.* (2014). The color version of this figure is available only in the electronic edition.

tion (13). We have applied this method to 13 small events (**M** −7 to **M** −5.5) reported in Table 1. $C_{F\dot{M}}$ estimates range from 3 to 26 km/s with a median value of 7.5 km/s, which is in good agreement with our theoretical estimate (7 km/s), based on the wavespeed of the granite.

Source Dimension, Stress Drop, and Radiated Energy

Many of the general features of the source spectra of AEs and other laboratory-generated seismic events are similar to those expected for natural earthquakes. At low frequencies, spec-

tra are approximately flat, and at high frequencies they fall off at a rate close to f^{-2}. The larger events have corner frequencies that are well within our reliable frequency band, permitting us to estimate source dimension, stress drop, and radiated energy.

We assume the Brune (1970) relationship between f_0 and source dimension $r_0 = 2.34 \times \beta/(2\pi f_0)$ and calculate stress drop $\Delta\sigma = 7/16M_0 r_0^{-3}$. To estimate radiated energy E_s, we extrapolate the low-frequency level of $\dot{M}(f)$ to low frequencies and the f^{-2} fall-off to high frequencies and then follow equation (16) of Singh and Ordaz (1994),

Table 2
Properties of Laboratory-Generated Seismic Events from Experiments on the Large Biaxial Apparatus

Event Name	σ_n (MPa)	Distance Along Strike (m)	Depth (m)	From Waveform Modeling					From Spectral Fitting			$C_{F\dot{M}}$ (km/s)
				t_0 (μs)	$\dot{m}_{\max}$ (kN·m/s)	M_0 (N·m)	$\Delta\sigma$ (Mpa)	**M**	Δp_{equiv} (N·s)	$\Delta\sigma$ (MPa)	**M**	
SE2Jan2012 FS-17 (P4)	5	1.2	0.29	3	60	0.1	1.6	−6.7	1.3×10^{-5}	0.3	−6.8	7.9
SE12Jan2012 FS-43 (P1)	5	1	0.29	n/a	n/a	n/a	n/a	n/a	1.0×10^{-2}	0.05	−4.8	n/a
SE2Jan2012 FS-33 (P1)	5	1	0.29	n/a	n/a	n/a	n/a	n/a	1.6×10^{-2}	0.12	−4.7	n/a
SE7Jan2012 FS-20 (P1)	5	1.01	0.29	n/a	n/a	n/a	n/a	n/a	2.4×10^{-2}	0.12	−4.6	n/a
SE12Jan2012 FS-34 (P2)	5	1.09	0.32	3	250	0.4	6.7	−6.3	2.0×10^{-5}	1	−6.6	20.9
SE12Jan2012 FS-46 (P0.5)	5	1	0.34	9.5	174	0.9	0.5	−6.1	3.6×10^{-5}	0.03	−6.5	25.8
SE12Nov2012 FS-46	4	0.5	0.40	3.5	430	0.8	8.4	−6.1	1.6×10^{-4}	0.03	−6.0	5.3
SE12Nov2012	4	n/a	n/a	n/a	n/a	n/a	n/a	n/a	1.6×10^{1}	0.37	−2.7	n/a
SE12Nov2012 AS+49	4	1.24	0.17	5	300	0.8	2.9	−6.1	1.2×10^{-4}	0.61	−6.1	7.0
SE16Nov2012 FS-17	6	1.25	0.38	4.5	2160	5.4	25.5	−5.6	8.0×10^{-4}	3	−5.6	6.8
SE17Nov2012	6	n/a	n/a	n/a	n/a	n/a	n/a	n/a	2.6×10^{1}	1.4	−2.6	n/a
SE26Nov2012 FS-85	6	0.63	0.36	5.5	3700	11	29.3	−5.4	1.0×10^{-3}	4	−5.5	11.3
SE26Nov2012 FS-39	6	1.26	0.33	5	84	0.2	0.8	−6.5	2.9×10^{-5}	0.5	−6.5	8.1
SE26Nov2012 FS-5	6	1.66	0.19	5.5	300	0.9	2.4	−6.1	2.0×10^{-4}	1.5	−6.0	4.6
SE26Nov2012 AS+48	6	1.31	0.23	4.5	25	0.06	0.3	−6.9	2.0×10^{-5}	1	−6.6	3.1
SE26Nov2012 FS-27	6	1.43	0.11	3	25	0.04	0.7	−7.0	5.6×10^{-6}	0.04	−7.0	7.5
SE25Nov2012 FS-148	6	−0.38	0.36	4.5	3600	9.0	42.6	−5.4	1.0×10^{-3}	6	−5.5	9.0
SE25Nov2012 FS-53	6	−0.4	0.26	4	180	0.4	2.7	−6.3	6.3×10^{-5}	2	−6.3	6.4

Columns are, from left to right: event name, fault average normal stress, location of the event along strike, depth of the event, width of $\dot{m}(t)$, height of $\dot{m}(t)$, seismic moment derived from t_0 and $\dot{m}_{\max}$, stress drop derived from t_0 and M_0, magnitude derived from M_0, equivalent change in momentum from spectral fitting, stress drop from spectral fitting, magnitude derived from Δp_{equiv} assuming $C_{F\dot{M}} = 7$ km/s, and scale factor derived from Δp_{equiv} and M_0. The event naming scheme is consistent with Figure 3 and McLaskey et al. (2014).

$$E_s = \frac{4\pi}{5\rho\beta^5} \int_0^\infty f^2 \dot{M}(f)^2 df, \qquad (22)$$

in which, for the granite, the shear-wave velocity $\beta = 2700$ m/s, density $\rho = 2670$ kg/m^3, and shear modulus $\mu = 20$ GPa. From E_s, we calculate apparent stress $\tau_a = \mu E_s / M_0$ and scaled energy $\tilde{e} = E_s / M_0$. (Equation 22 is strictly valid only for spectra derived from S waves whereas spectra reported in this article are obtained from windows that include both P and S waves. Because most of the radiated energy is contained in the S waves, we believe this discrepancy is minor.)

The largest AE events (**M** −4.5) with rupture areas that are contained within the interior of the fault are well fit by the Brune model. They have 0.1 MPa stress drops, estimated source radii of ~80 mm, and about 1×10^{-4} J of radiated energy. For many of the smaller events, the corner frequency implied by fitting with the Brune model is close to the upper limit of our reliable frequency band (200 kHz), so source parameters are not well constrained. If the Brune models shown in Figure 8b are appropriate, they imply stress drops of about 0.05–5 MPa, and source dimensions of 3–10 mm, as described in Table 2. We believe that the large variation in stress drops is an accurate reflection of the variability of AEs produced by this sample, because the two methods (waveform modeling and spectral fitting) produced similar results. On average, though, the stress drops derived from spectral fitting are about a factor of 10 lower than those estimated from waveform modeling (Table 2), and this systematic difference may indicate bias in one or both of the two methods.

Source spectra from the stick-slip events that rupture the entire fault appear to have deficient spectral amplitudes near the corner frequency and have a somewhat more variable fall-off at higher frequencies (2 kHz $< f <$ 200 kHz), though f^{-2} is still an adequate approximation. These differences are likely due to edge effects and because the stick-slip events are controlled by the stiffness of the apparatus rather than the rigidity of the rock. This topic will be the focus of a future study.

Discussion

Instrument Response from $\Psi^{\text{ext}}(f)$

If we assume that the spectra of the Green's functions $G_{ki}^{\text{ext}}(f)$ are approximately flat, then the shape of the instrument-apparatus response $\Psi^{\text{ext}}(f)$ is controlled primarily by instrument distortions $I_k(f)$. In this case, we can use our estimates of instrument-apparatus response to make statements about the general features of a sensor's response spectrum such as whether sensor output is proportional to displacement, velocity, or acceleration. We believe that the above approximation may be appropriate (at least to a factor of 10) for the two experimental configurations described in this article because there is no obvious resonance of the sample in our frequency band. Our results suggest that the sensors in the triaxial apparatus behave approximately as accelerometers ($\Psi^{\text{ext}}(f)$ has a slope of ~40 dB/decade) in the 20–200 kHz frequency band. Similarly, the Panemetrics sensors used on the biaxial apparatus behave approximately as accelerometers

in the 2–20 kHz frequency band and approximately as displacement sensors in the 20–200 kHz band.

Careful analysis of Figures 8 and 9 show that the distinctive notch in the spectra at 20 kHz visible in Figures 8a,b and 9a, is likely due to an antiresonance in the Panametrics V103 sensor response, and it is effectively removed in Figures 8c and 9b. In addition, Figure 8a shows an apparent corner frequency f_0 for the largest events around 10 kHz, but this is an artifact introduced by a bend in the instrument-apparatus response spectrum $\Psi^{\text{ext}}(f)$ at that frequency. The true f_0 is closer to 1 kHz as depicted in Figure 9b.

Applicability of $\Psi^{\text{int}}(f) = C_{F\dot{M}} \Psi^{\text{ext}}(f)$

For the triaxial apparatus, the similarity in slope and shape of the spectra in Figure 4b gives us confidence that equation (16) ($\Psi^{\text{int}}(f) = C_{F\dot{M}} \Psi^{\text{ext}}(f)$) is at least approximately appropriate. We also compared spectral estimates from AEs that were not collocated with the ball impact. In general, we found only about 10 dB variations in the 5–400 kHz frequency band considered. This indicates that, for this experiment, the amplitude of the instrument-apparatus response spectrum ($|\Psi^{\text{int}}(f)|$) is insensitive to ∼100 mm changes in source location, as long as spectra are obtained from the averages of many sensors' signals.

For the large biaxial apparatus, we studied the variability of $|\Psi^{\text{ext}}(f)|$ as a function of different ray paths and with different source and sensor locations. We found three main factors that can significantly affect spectral estimates. First, signals recorded from sensors on the same surface as the ball impact location have large amplitude Rayleigh waves and enhanced high-frequency content (by 10–40 dB in the 20–100 kHz range) relative to signals the ray paths of which traverse the thickness of the sample. Second, ray paths that traverse the fault (even with the applied 5 MPa normal stress) have spectra that are diminished 5–10 dB in a frequency band above ∼50 kHz. Third, at frequencies higher than about 20 kHz, ∼100 mm variations in ray-path lengths also bias $|\Psi^{\text{ext}}(f)|$ estimates by a maximum of ∼20 dB at the highest frequencies (200 kHz). To avoid these three cases, $\Psi^{\text{ext}}(f)$ was calculated only from signals with ray paths that traverse the thickness of the sample (thus eliminating Rayleigh waves) but do not traverse the fault. In addition, we derived raw spectra of both AEs and ball impact from recordings from sets of sensors with similar ray-path lengths and takeoff angles, as depicted in Figure 7. This approach works well for smaller events, but for the large stick-slip events that rupture the entire simulated fault, the source is distributed and path lengths and takeoff angles are only grossly approximated. We estimate that, using the above techniques, $|\Psi^{\text{ext}}(f)|$ of the large stick-slip events is accurate to ±10 dB in the ∼2–200 kHz frequency band considered. Accuracy of spectral estimates of the smaller events is probably better.

For $f < 1$ kHz, wavelengths are longer than the sample dimensions, and all sources are approximately collocated. In this frequency range, spectral differences between different source and sensor locations are likely due to resonance of the sample and apparatus. Laboratory-generated seismic events and ball impact likely excite somewhat different resonant modes, yet we do not find any indication that such modes are dominant enough to severely affect the spectra. In total, we believe that errors associated with $\Psi^{\text{int}}(f) = C_{F\dot{M}} \Psi^{\text{ext}}(f)$ probably cause the ±10 dB deviations from theoretical source spectra shown in Figure 9b compared to ±4 dB deviations in Figure 8c. Because the frequency band considered is relatively wide, estimates of general features of $\dot{M}(f)$ such as the low-frequency level M_0, and the high-frequency falloff are still relatively robust despite the ±10 dB uncertainty in individual spectral estimates.

Assumptions and Uncertainty

In many ways, the empirical technique is simpler than other calibration techniques, and we believe that moment estimates derived from this calibration scheme are robust. For example, the calibration is performed *in situ*, and we make no assumptions about reciprocity, sensor coupling, sensor aperture effects, or inelastic wave propagation effects such as attenuation and scattering. Modeling of wave propagation is not required, so the calibration can be extended to lower frequencies that are more difficult to model for small samples or complicated geometries. Finally, for the experiments on the large biaxial apparatus, we used only the ball drop spectra in a frequency band below the corner frequency, so the accuracy of the method does not rely on the validity of Hertz theory of impact.

Instead, the empirical calibration technique relies on different simplifying assumptions such as the minimization of radiation pattern effects by averaging over multiple ray paths and the applicability of $\Psi^{\text{int}}(f) = C_{F\dot{M}} \Psi^{\text{ext}}(f)$ (equation 16), as described in the previous section. We estimate that these assumptions cause uncertainty of individual spectral estimates to be about ±10 dB. Uncertainty in moment estimated from the low-frequency level of these spectra will depend on the location of the corner frequency with respect to the reliable frequency band, but for most of the events shown in Figure 9 and reported in Table 2, we believe moment estimates are accurate to ±6 dB, or ±0.2 magnitude units. Uncertainty from variation in ball impacts is on the order of ±1 dB (for frequencies below the corner frequency) and is therefore small compared to other sources of uncertainty.

There are additional uncertainties associated with the calculation of $C_{F\dot{M}}$ such as the free surface effect, which is approximated by $g_{ki}^{\text{ext}}(t) \approx 2g_{ki}^{\text{int}}(t)$ for normal incidence (equation A5), the wave velocity (equation A7), and the averaging of radiation patterns ($X_j \equiv \Xi_i / \Lambda_{ij} \approx 1$). We estimate that these approximations could introduce an additional factor of two (6 dB) uncertainty but are probably small compared to the uncertainties in spectral estimates described above.

Despite the approximations, we believe that the methods and results described here indicate that the ball impact empirical calibration technique can serve as an effective method

of obtaining absolute moment to within $\pm$ a factor of two (± 0.2 magnitude units). A similar technique that employs a more massive ball might be adapted for absolute calibration of microseismic networks in mines.

Conclusion

We have demonstrated a method to determine the absolute moment of AEs and other laboratory-generated seismic events with an uncertainty of ± 0.2 magnitude units. The advantage of this method is that it is performed *in situ*, and no modeling of wave propagation or assumptions about attenuation or sensor coupling are required. The method relies on the principle of an empirical Green's function, but instead of using a small, collocated seismic event of unknown absolute magnitude, the method employs a ball impact as a well-defined reference source.

The ball impact source occurs on the external surface of the sample and is represented by forces, whereas most seismic events occur within the interior of a sample (or the earth) and are represented by force couples that are quantified by their seismic moment. To quantitatively relate these two classes of sources, we derived equations that link the seismic moment of an internal source (i.e., earthquake, acoustic emission, or underground explosion) to the change in momentum of an external source (i.e., a ball impact or meteor impact). We found that for frequencies that are sufficiently below the corner frequencies, these sources are related by a constant, $C_{F\dot{M}}$, which is equal to twice the speed of sound in the material from which the sources originate.

We demonstrate the calibration method for two different rock deformation experiments. These experiments employ different loading frames, samples, stress levels, and recording equipment. The first experiment demonstrates the *in situ* calibration of an AE monitoring system under 40 MPa confining pressure. In the second experiment, a 2 m long fault in a biaxial loading configuration is used to generate a collection of seismic events that are analyzed both by the current method and by means of waveform modeling, which is described elsewhere. This comparison is used to empirically validate the theory. In addition to seismic moment, the calibration technique facilitates the estimation of other seismic source parameters such as source dimension, stress drop, and radiated energy. The methodology described here provides a foundation for future studies that may explore how these seismic source parameters relate to other physical variables such as stress levels, fault surface roughness, and loading conditions.

Data and Resources

Data used in this article were acquired during laboratory experiments at the U.S. Geological Survey in Menlo Park, California. Data can be made available by request.

References

Aki, K. (1967). Scaling law of seismic spectrum, *J. Geophys. Res.* **72,** 1217–1231.

Aki, K., and P. G. Richards (1980). *Quantitative Seismology: Theory and Methods*, Freeman, San Francisco, California, 27–59.

Baltay, A., G. Prieto, and G. C. Beroza (2010). Radiated seismic energy from coda measurements and no scaling in apparent stress with seismic moment, *J. Geophys. Res.* **115,** no. B08314, doi: 10.1029/2009JB006736.

Bowers, D., and J. Hudson (1999). Defining the scalar moment of a seismic source with a general moment tensor, *Bull. Seismol. Soc. Am.* **89,** 1390–1394

Bracewell, R. (2000). *The Fourier transform and its applications*, Third Ed., McGraw-Hill, New York, New York, Chapter 6.

Brantut, N., A. Schubnel, and Y. Gueguen (2011). Damage and rupture dynamics at the brittle-ductile transition: The case of gypsum, *J. Geophys. Res.* **116,** no. B01404, doi: 10.1029/2010JB007675.

Brune, J. N. (1970). Tectonic stress and spectra of seismic shear waves from earthquakes, *J. Geophys. Res.* **75,** 4497–5009.

Dahm, T. (1996). Relative moment tensor inversion based on ray-theory: Theory and synthetic tests, *Geophys. J. Int.* **124,** 245–257.

Eitzen, D., and F. Breckenridge (1987). Acoustic emission sensors and their calibration, in *Nondestructive Testing Handbook*, Second Ed., R. Miller and P. McIntire (Editors), Vol. 5, Acoustic Emission Testing, American Society for Nondestructive Testing, Columbus, Ohio, 121–132.

Frankel, A., and H. Kanamori (1983). Determination of rupture duration and stress drop from earthquakes in southern California, *Bull. Seismol. Soc. Am.* **73,** 1527–1551

Goebel, T., T. Becker, D. Schorlemmer, S. Stanchits, C. Sammis, E. Rybacki, and G. Dresen (2012). Identifying fault heterogeneity through mapping spatial anomalies in acoustic emission statistics, *J. Geophys. Res.* **117,** B03310, doi: 10.1029/2011JB008763.

Goldsmith, W. (2001). *Impact*, Dover Publications, New York.

Goodfellow, S. D., and R. P. Young (2014). A laboratory acoustic emission experiment under in situ conditions, *Geophys. Res. Lett.* **41,** doi: 10.1002/2014GL059965.

Goujon, L., and J. C. Baboux (2003). Behavior of acoustic emission sensors using broadband calibration techniques, *Mes. Sci. Technol.* **14,** 903–908.

Grosse, C., and M. Ohtsu (2008). *Acoustic Emission Testing*, Springer-Verlag, Berlin, Germany.

Hanks, T. C., and H. Kanamori (1979). A moment magnitude scale, *J. Geophys. Res.* **84,** 2348–2350.

Hatano, H., and T. Watanabe (1997). Reciprocity calibration of acoustic emission transducers in Rayleigh-wave and longitudinal-wave sound fields, *J. Acoust. Soc. Am.* **101,** 1450–1455.

Hough, S. E., and D. S. Dreger (1995). Source parameters of the 23 April 1992 M 6.1 Joshua Tree, California, earthquake and its aftershocks: Empirical Green's function analysis of GEOS and TERRA scope data, *Bull. Seismol. Soc. Am.* **85,** 1576–1590.

Hsu, N., and F. Breckenridge (1981). Characterization and calibration of acoustic emission sensors, *Materials Eval.* **39,** 60–68.

Hutchings, W., and F. Wu (1990). Empirical Green's functions from small earthquakes: A waveform study of locally recorded aftershocks of the 1971 San Fernando earthquake, *J. Geophys. Res.* **95,** 1187–1214.

Kwiatek, G., K. Plenkers, and G. Dresen (2011). Source parameters of picoseismicity recorded at Mponeng Deep Gold Mine, South Africa: Implications for scaling relations, *Bull. Seismol. Soc. Am.* **101,** no. 6, 2592–2608, doi: 10.1785/0120110094.

Lei, X., O. Nishizawa, and K. Kusunose (1993). Band-limited heterogeneous fractal structure of earthquakes and acoustic-emission events, *Geophys. J. Int.* **115,** 79–84.

Lockner, D. A. (1993). Role of acoustic emission in the study of rock fracture, *Int. J. Rock Mech. Min. Soc. Geomech. Abstr.* **30,** 884–899.

McLaskey, G. C., and S. D. Glaser (2010). Hertzian impact: Experimental study of the force pulse and resulting stress waves. *J. Acoust. Soc. Am.* **128,** 1087–1096.

McLaskey, G. C., and S. D. Glaser (2012). Acoustic emission sensor calibration for absolute source measurements, *J. Nondest. Eval.* **31,** 157–168.

McLaskey, G. C., and B. D. Kilgore (2013). Foreshocks during the nucleation of stick-slip instability, *J. Geophys. Res* **118,** 2982–2997, doi: 10.1002/jgrb.50232.

McLaskey, G. C., and D. A. Lockner (2014). Preslip and cascade processes initiating laboratory stick-slip, *J. Geophys. Res.* **119,** doi: 10.1002/2014JB011220.

McLaskey, G. C., B. D. Kilgore, D. A. Lockner, and N. M. Beeler (2014). Laboratory generated M –6 earthquakes, *Pure Appl. Geophys.*, doi: 10.1007/s00024-013-0772-9.

Mogi, K. (1962). Magnitude-frequency relation for elastic shocks accompanying fractures of varios materials and some related problems in earthquakes, *Bull. Earthq. Res. Inst.* **40,** 831–853.

Mueller, C. S. (1985). Source pulse enhancement by deconvolution of an empirical Green's function, *Geophys. Res. Lett.* **12,** 33–36 doi: 10.1029/GL012i001p00033.

Oppenheim, A., A. Willsky, and I. Young (1983). *Signals and Systems*, Prentice-Hall, New Jersey.

Scholz, C. (1968). The frequency-magnitude relation of microfracturing in rock and its relation to earthquakes, *Bull. Seismol. Soc. Am.* **58,** 399–415.

Sellers, E. J., M. O. Kataka, and L. M. Linzer (2003). Source parameters of acoustic emission events and scaling with mining-induced seismicity, *J. Geophys. Res.* **108,** no. B9, 2418.

Singh, S. K., and M. Ordaz (1994). Seismic energy release in Mexican subduction zone earthquakes, *Bull. Seismol. Soc. Am.* **84,** 1533–1550.

Stump, B., and L. Johnson (1977). The determination of source properties by the linear inversion of seismograms, *Bull. Seismol. Soc. Am.* **67,** 1489–1502.

Appendix A

This appendix outlines a theoretical derivation of the force-moment-rate constant $C_{F\dot{M}}$ that relates the force-time function of an external seismic source (ball impact) to the moment-rate function of an internal seismic source (acoustic emission [AE] or earthquake). We start by substituting equation (4) into equation (2). Noting that $m_{ij}(t) \otimes g_{ki,j}^{int}(t) = \dot{m}_{ij}(t) \otimes \int g_{ki,j}^{int}(t) dt$, we find

$$\dot{m}(t) = s^{int}(t) \otimes (i_k^{int}(t) \otimes \Lambda_{ij} \int g_{ki,j}^{int}(t) dt)^{-1}. \qquad (A1)$$

Similarly, by substituting equation (5) into equation (3), we find

$$f(t) = s^{ext}(t) \otimes (i_k^{ext}(t) \otimes \Xi_i g_{ki}^{ext}(t))^{-1}. \qquad (A2)$$

We substitute the above two equations into equation (13),

$$C_{F\dot{M}} = \frac{s^{int}(t) \otimes i_k^{ext}(t) \otimes g_{ki}^{ext}(t) \Xi_i}{s^{ext}(t) \otimes i_k^{int}(t) \otimes \int g_{ki,j}^{int}(t) dt \Lambda_{ij}}. \qquad (A3)$$

We choose a geometry such that the path length and angle of incidence is similar between internal and external sources such that $i_k^{ext}(t) = i_k^{int}(t)$. Then, we substitute

$u_k^{int}(t) = s^{int}(t) \otimes i_k^{int}(t)$ and $u_k^{ext}(t) = s^{ext}(t) \otimes i_k^{ext}(t)$ into the above equation and recall that equation (13) only holds for the special case when $u_k^{ext}(t) = u_k^{int}(t)$, to find

$$C_{F\dot{M}} = \frac{X_j g_{ki}^{ext}(t)}{\int g_{ki,j}^{int}(t) dt}, \qquad (A4)$$

in which $X_j = \Xi_i / \Lambda_{ij}$. Given the similar geometry noted above, we make the approximation

$$g_{ki}^{ext}(t) \approx 2 g_{ki}^{int}(t), \qquad (A5)$$

in which the factor of 2 comes from the free surface amplification. This approximation will certainly be violated if Rayleigh waves or other surface waves have a major contribution to $g_{ki}^{ext}(t)$. Substituting equation (A5) into equation (A4), we find

$$C_{F\dot{M}} = \frac{X_j g_{ki}^{ext}(t)}{\int d(g_{ki}^{ext}(t)/2)/dx_j dt} \approx 2 X_j \frac{dx_j}{dt}. \qquad (A6)$$

If we minimize the effect of radiation patterns by averaging over multiple stations with good coverage of the focal sphere, then $X_j \approx 1$. In this case, equation (A6) becomes two times the wave velocity in the material. If spectral estimates are derived from a section of recorded signals that includes only one particular wave phase (i.e., *P* wave) then the velocity of that wave phase should be used in equation (A6). In the current case, spectra are derived from sections of recorded signals that include *P* and *S* waves, so we choose the average of the *P*- and *S*-wave velocities:

$$C_{F\dot{M}} \approx 2(c_P + c_S)/2. \qquad (A7)$$

Here, we also assume that the granite is approximately isotropic. These assumptions could introduce additional uncertainty of at most a factor of two.

U.S. Geological Survey
Earthquake Science Center
345 Middlefield Road MS 977
Menlo Park, California 94025
gcm8ster@gmail.com
    (G.C.M., D.A.L., B.D.K.)

U.S. Geological Survey
Cascades Observatory
1300 Cardinal Court
Building 10 Suite 100
Vancouver, Washington 98683
    (N.M.B.)